# Stability of superconducting resonators: Motional narrowing and the role of Landau-Zener driving of two-level defects

N.B. When citing this work, cite the original published paper.

(article starts on next page)

CONDENSED MATTER PHYSICS

# Stability of superconducting resonators: Motional narrowing and the role of Landau-Zener driving of two-level defects

David Niepce[1]*, Jonathan J. Burnett[2], Marina Kudra[1], Jared H. Cole[3], Jonas Bylander[1]*

Frequency instability of superconducting resonators and qubits leads to dephasing and time-varying energy loss and hinders quantum processor tune-up. Its main source is dielectric noise originating in surface oxides. Thorough noise studies are needed to develop a comprehensive understanding and mitigation strategy of these fluctuations. We use a frequency-locked loop to track the resonant frequency jitter of three different resonator types— one niobium nitride superinductor, one aluminum coplanar waveguide, and one aluminum cavity—and we observe notably similar random telegraph signal fluctuations. At low microwave drive power, the resonators exhibit multiple, unstable frequency positions, which, for increasing power, coalesce into one frequency due to motional narrowing caused by sympathetic driving of two-level system defects by the resonator. In all three devices, we identify a dominant fluctuator whose switching amplitude (separation between states) saturates with increasing drive power, but whose characteristic switching rate follows the power law dependence of quasi-classical Landau-Zener transitions.

## INTRODUCTION

Superconducting microwave resonators (1), in a variety of geometries, are essential tools in circuits for quantum computing (2), microwave quantum optics (3), low-noise amplifiers (4), radiation detectors (1), and particle accelerators (5, 6). While the reduction of energy loss of resonators and qubits has received remarkable attention (1, 2, 7), leading to long-lived qubits (8, 9) and high-quality resonators (10), far fewer studies report on parameter fluctuations (9, 11–13). Such fluctuations present a challenge to the bring-up and calibration stability of current quantum processors (14). Thorough noise studies are needed to understand and mitigate these fluctuations. Here, we examine the low-frequency jitter of three different types of superconducting resonator with the same experimental setup and observe notably similar random telegraph signal (RTS) fluctuations. At low excitation power, the RTS lead to multiple quasi-stable frequency positions that coalesce at high powers, which we interpret as motional narrowing caused by direct (sympathetic) driving of individual two-level system (TLS) defects by the resonator field, causing Landau-Zener transitions between the TLS states.

While the community agrees on the many underlying decoherence mechanisms that contribute to decoherence, it remains divided on the relative importance of each mechanism. For example, the dissipation within Al resonators has been separately found to be limited by free-space photon-generated quasiparticles (15) and two-level defects (16). Similarly, dissipation in granular aluminum oxide resonators has been separately found to be limited by non-equilibrium quasiparticles (17) and also by two-level defects (18). Untangling these effects is complicated by experimental details that often differ: different signal filtering, use of infrared absorber,

magnetic shielding, and circuit board enclosure versus cavity enclosure. These differences make reports difficult to directly compare, resulting in conflicting interpretations of the underlying mechanism. This clearly demonstrates the need for experiments with common experimental details and for the standardization of measurement techniques.

Here, we specifically use an identical measurement and analysis infrastructure to compare three very distinct types of superconducting resonators: an NbN ($T_c$ = 7.2 K) 20-nm-thick nanowire superinductor (19), an Al ($T_c$ = 1.05 K) 150-nm-thick coplanar resonator, and finally an Al ($T_c$ = 1.18 K) millimeter-scale three-dimensional (3D) cavity resonator (20). The device characteristics are summarized in Table 1 and in Materials and Methods. All three devices have similar resonant frequencies $f_r$ but vastly different superconducting properties, electric field distributions, kinetic inductance fractions, and internal quality factors $Q_i$. By performing the same detailed analysis of the frequency jitter of these devices as a function of drive power, we are able to directly compare the noise characteristics of all three devices.

A key observation is that the frequency response of these devices fluctuates as an RTS, i.e., the frequency switches instantaneously between two or more discrete levels—see Fig. 1A. As the devices differ greatly in terms of design and dimensions, we attribute these fluctuations to TLS defects, omnipresent in the dielectrics of superconductor surfaces and interfaces. Dielectric loss, due to near-resonant TLS, is a limiting factor for resonator internal quality

[1]Chalmers University of Technology, Microtechnology, and Nanoscience, SE-41296 Gothenburg, Sweden. [2]National Physical Laboratory, Hampton Road, Teddington Middlesex TW11 0LW, UK. [3]Chemical and Quantum Physics, School of Science, RMIT University, Melbourne, VIC 3001, Australia.
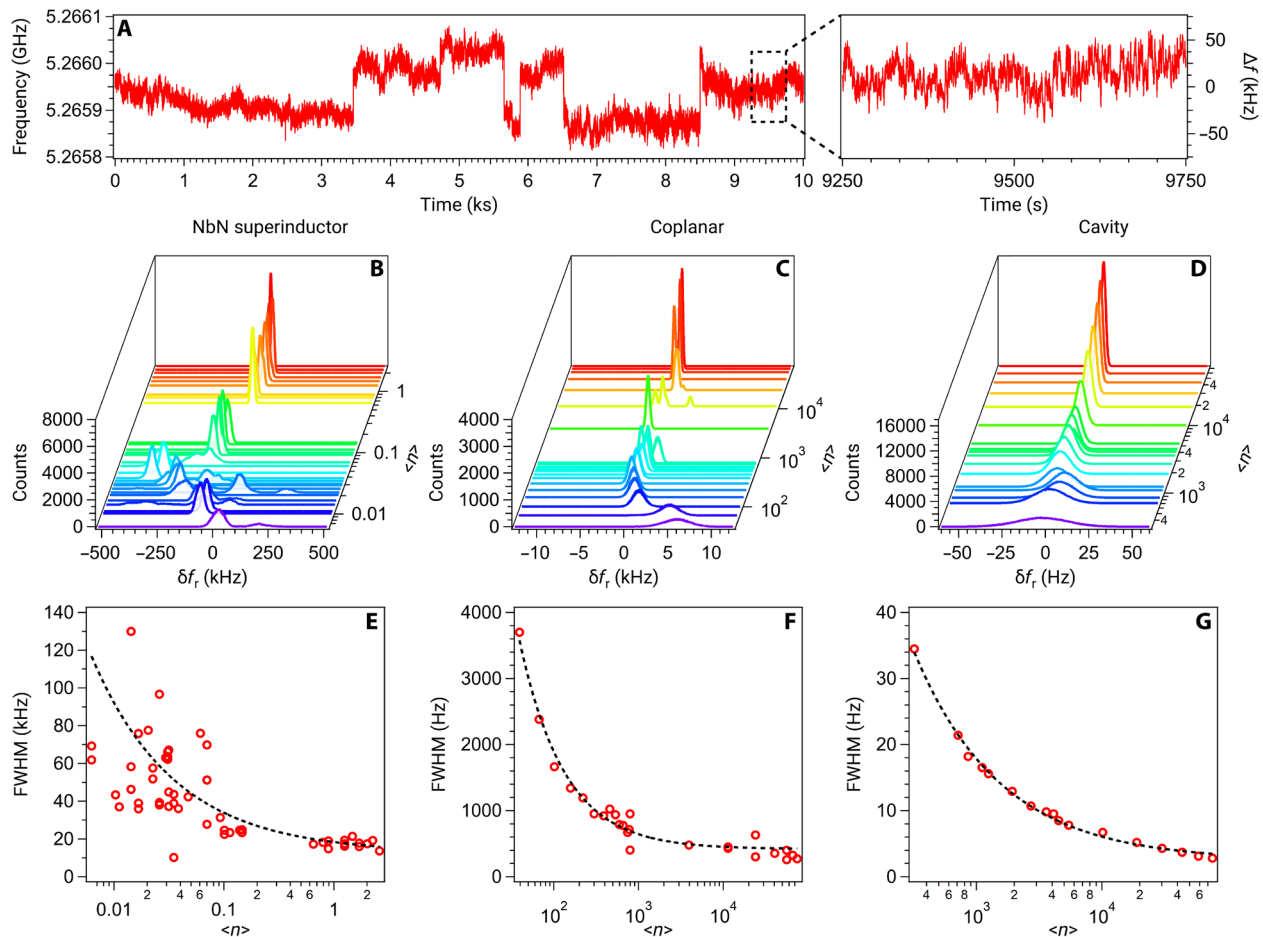*Corresponding author. Email: david.niepce@chalmers.se (D.N.); jonas.bylander@chalmers.se (J.B.)

**Table 1. Characteristics of the three resonators.**

| Resonator | $f_r$ (GHz) | $Z_c$ (ohm) | $Q_i$ | $Q_c$ |
|---|---|---|---|---|
| Nanowire (19) | 5.3 | $6.8 \times 10^3$ | $2.5 \times 10^4$ | $8.0 \times 10^4$ |
| Coplanar (61) | 4.3 | 50 | $5.4 \times 10^5$ | $1.8 \times 10^5$ |
| Cavity (20) | 6.0 | 58 | $1.1 \times 10^7$ | $8.2 \times 10^6$ |

**Fig. 1. Resonator frequency fluctuations.** (**A**) Raw frequency jitter of the nanowire resonator sampled at 100 Hz, at an applied power corresponding to an average number of $\langle n \rangle \simeq 3 \times 10^{-2}$ photons in the resonator. (**B** to **D**) Histograms of the frequency fluctuations for the three resonators versus applied power. The data are normalized to the mean frequency of the highest applied power. (**E** to **G**) Peak widths [full width at half maximum (FWHM)] of the data in (B) to (D). (Note that FWHM refers to the width of one peak in the histogram and not to the distance between resolvable peaks that correspond to quasi-stable configurations.)

factors, qubit relaxation times ($T_1$), microwave kinetic inductance detector detection efficiencies (1), and accelerator cavity efficacies (5, 6). Simultaneously, dielectric noise, due to low-frequency TLS, leads to spectral instability, i.e., fluctuations of $T_1$ (typically by 20%) and of qubit frequencies (typically by a few kilohertz) with concomitant dephasing. The observed noise response reported here is entirely consistent with recent reports on fluctuations of single TLS or few TLS defects within superconducting qubits (9, 11–13); however, in this setup, we are able to go further and identify the characteristics of a dominant TLS and even differentiate between device-specific response revealing TLS behavior, which is unexpectedly consistent across devices. Analysis of the temporal fluctuations by spectral density and, particularly, by Allan deviation techniques offers a window into the dynamics. As a result, we attribute the observed power dependence to sympathetic driving of the TLS bath by the resonator field. Then, by analyzing the fluctuations, we find that the RTS switching rate of all resonators follows a common power law dependence that is consistent with the quasi-classical expression for the Landau-Zener transition rate. We make no claim to know the microscopic identity of the TLS, for which there is a multitude of proposed mechanisms (7): Besides charged

defects, there are hybridized models in which material defects couple to the superconducting state in various ways (21–24).

## RESULTS

### Temporal frequency fluctuations

We use a Pound frequency–locked loop to measure the fluctuations of $f_r$ of the resonators for 2 hours and 45 min (see Materials and Methods). Figure 1A shows an example of such a dataset. We observe that the frequency fluctuates between discrete points, as is characteristic of an RTS. These fluctuations occur at all observable time scales, as can be seen in the inset over a much shorter time period.

To qualitatively compare between the different devices, we calculate the histogram of frequency fluctuations measured on each of the resonators against circulating power in units of the average photon occupation number $\langle n \rangle$ (Fig. 1, B to D) and extract the histogram full width at half maximum (FWHM) (Fig. 1, E to G). We observe that the fluctuation amplitude (histogram width) is the highest for the nanowire resonator (Fig. 1, B and E), lower in the coplanar resonator (Fig. 1, C and F), and lowest in the cavity

(Fig. 1, D and G). We attribute this to fluctuations of the real part of the dielectric susceptibility, which acts as an effective capacitance noise on the resonator and therefore leads to frequency fluctuations. The nanowire has the highest sensitivity to electric fields due to its very high impedance and high electric field filling factor (*19*, *25*). In the coplanar resonator, the electric field is not as strongly coupled. Last, the cavity has the smallest filling factor and will therefore exhibit the least amount of frequency fluctuations. We note that, while the losses of superconducting cavities have been studied at sub-kelvin temperatures (*5*, *6*, *20*, *26*), we have found no reports of frequency noise of superconducting cavities at these temperatures.

Qualitatively, Fig. 1 (B to D) demonstrates all the hallmarks of motional narrowing due to one or more RTS fluctuators (*27–31*). At low power, we see multiple frequency positions, which can be attributed to several slowly varying RTS signals. If we were to continue measuring for even longer time periods, then we would ultimately expect a Gaussian distribution of frequency shifts (*31*). As the power is increased, these peaks coalesce into a single distribution whose width narrows as the power increases. To obtain an estimate for the power dependence of this narrowing, we fit the FWHM, shown via the dashed lines in Fig. 1 (E to G), to the functional form $F_0 + F_1/\langle n \rangle^\beta$, and we find a β values of 0.58, 0.82, and 0.63 for the nanowire, resonator, and cavity, respectively (see table S1 and discussion in the Supplementary Materials).

## Spectral and Allan analysis of fluctuations: Universal dependence of individual RTS fluctuators on the applied drive power

To gain further insight into the fluctuations, we examine the spectral properties (Fig. 2A) and Allan deviation (Fig. 2B) of the frequency fluctuations. While the frequency spurs in the time series data in Fig. 1A are indicative of RTS noise, the spectral and Allan responses allow us to quantitatively fit the data and identify the unique characteristics of an RTS response (*32*), in contrast to other types of noise (e.g., "white" or $1/f$). The data in Fig. 2 prominently features a single dominating RTS fluctuator (see Materials and Methods and Eqs. 7 and 8 for the functional form), which we can fit to extract its amplitude $A$, corresponding to a frequency step size between the states of the telegraph noise process, and characteristic time $\tau_0$.

We analyze the fluctuation data for a range of drive powers, shown in fig. S1, and we observe that all three devices present similar noise profiles—featuring one dominant RTS fluctuator—albeit at widely different amplitudes: The nanowire is the noisiest, and the cavity is the quietest. In general, there exist other less-prominent RTS features, sometimes at sufficient densities that they sum up to a $1/f$-like trend (*33*). In the limit of few RTS fluctuators, or alternatively in the $1/f$ limit, the data can be reliably fitted. However, between these limits, it becomes nontrivial to determine the exact number of RTS fluctuators that describe the fluctuations. For consistency, we therefore focus on determining the characteristic switching time $\tau_0$ and amplitude $A$ of the dominant RTS fluctuator within our measurement window and plot the resulting values of $A$ and $\tau_0$ versus $\langle n \rangle$ in Fig. 3 (A and B), respectively.

When examining the raw frequency jitter (Fig. 1A), an initial assumption would be that the noise present is a mixture of RTS (on ~100-s time scale) and white frequency noise (i.e., $S_y \propto f^0$ and $\sigma_y \propto \tau^{-0.5}$). However, from the power spectral density (PSD) and Allan deviation methods, it is clear that no white frequency noise is present (in the Supplementary Materials, this is shown for all
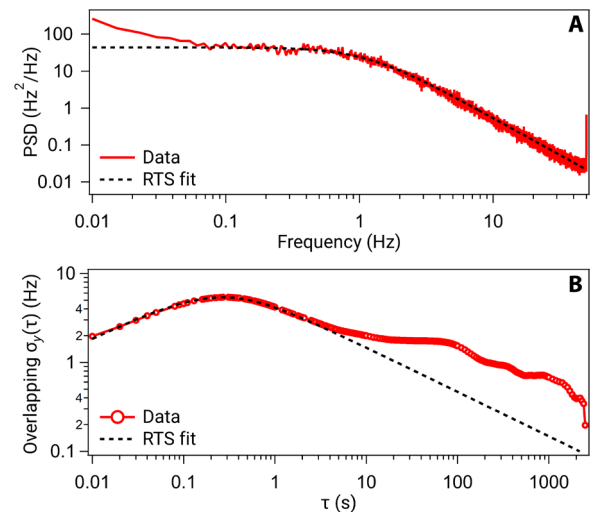


**Fig. 2. Fitting of the noise to an RTS fluctuator model.** (**A**) Example of a Welch power spectral density $S_y(f)$ and (**B**) overlapping Allan deviation $\sigma_y(\tau)$ for the measured frequency fluctuation data from the cavity resonator held at $T = 10$ mK and with an applied microwave drive power $P = -131.5$ dBm ($\langle n \rangle \simeq 715$). The data were sampled at 100 Hz. The dashed line corresponds to a fit of the RTS fluctuator feature using a common set of fitting parameters for both traces (Eqs. 7 and 8). The data below 0.1 Hz (above 10 s) represent the tail of one or several secondary RTS fluctuators (see Discussion).

microwave drives). Therefore, the noise present is a combination of an RTS at time scales of ~100 s and other RTS at much smaller time scales of ~1 ms to 1 s (see Fig. 3B). Hence, the multipeak behavior of Fig. 1 (B to D) occurs because of the longer time scale RTS, whereas the width in Fig. 1 (E to G) is determined by the smaller time scale RTS. Within our measurement window, the shorter time scale RTS dominates the signal, from which we extract the parameters $A$ and $\tau_0$.

In Fig. 3A, we see that $A$ is initially power dependent, decreasing with increasing power. However, it saturates at high powers, starting at a photon number corresponding approximately to the coalescence of peaks in Fig. 1 (B to D) ($\langle n \rangle \sim 0.1$ for the nanowire and $10^4$ for the cavity; here, we emphasize that the conversion from photon occupation to electric field is very different for each resonator). All three devices show this behavior, although the amplitudes, saturation levels $A_0$ (see Table 2), and the crossover points vary.

Furthermore, as shown in Fig. 3B, we find that the extracted $\tau_0$ values of the three resonators follow an empirical power law

$$\tau_0(\langle n \rangle) = (1 \text{ s}) \times (\langle n \rangle/n_1)^{-\alpha} \qquad (1)$$

where α is found close to 1.1 in all three resonators, and $n_1$ is a "critical" photon number for which $\tau_0 = 1$ s, unique for each device; see the fit parameters in Table 2. We note that $n_1$ determined in this way is not the same as the usual critical photon number, often denoted $n_c$, observed in measurements of dielectric loss (see the Supplementary Materials), which indicates the saturation of resonantly driven TLS.

## DISCUSSION

The power dependence of the histogram width and the noise characteristics revealed by the Allan deviation can be understood in
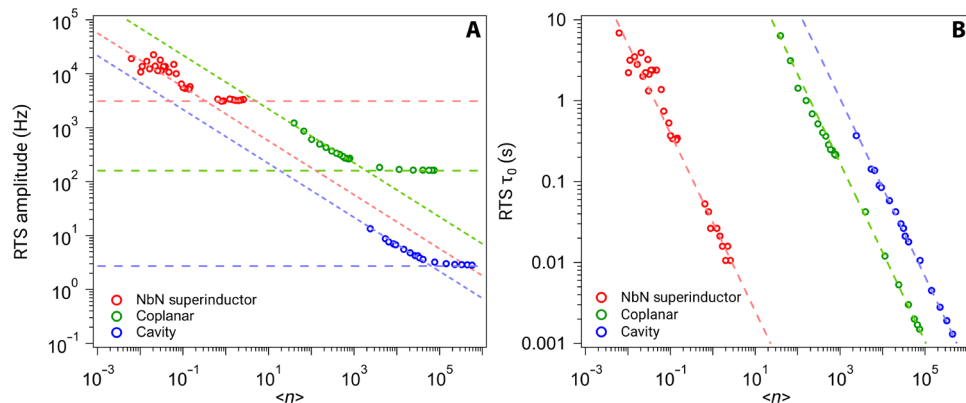
**Fig. 3. Analysis of the RTS.** (**A**) Drive-power dependence of the RTS amplitude $A$ and (**B**) switching time constant $\tau_0$ determined from noise data from the three resonators (fig. S1) fitted to the RTS model (Eq. 8). The horizontal dashed lines in (A) indicate the saturation $A \to A_0$, related to the minimum FWHM in Fig. 1 (E to G); the diagonal lines in (A) indicate $1/\sqrt{\langle n \rangle}$ scaling (not a fit). The dashed lines in (B) are fits of $\tau_0$ to the power law $(\langle n \rangle / n_1)^{-\alpha}$ (Eq. 1), with $\alpha = 1.1$. The fitted parameters are presented in Table 2.

**Table 2. Fit parameters for the dominant RTS fluctuators' switching times $\tau_0$ versus drive power $\langle n \rangle$ (Eq. 1) and saturation values ($A_0$) of their amplitudes $A$ for large $\langle n \rangle$, shown in Fig. 3.** The FWHM values refer to the histograms in Fig. 1 (E to G) at high power.

| Device | RTS $\tau_0$ | RTS $A$ |
|---|---|---|
| Nanowire | $\alpha = 1.1$ | $A_0 = 2.8 \times 10^3$ Hz |
| | $n_1 = 4.3 \times 10^{-2}$ | FWHM = $1.2 \times 10^4$ Hz |
| Coplanar | $\alpha = 1.1$ | $A_0 = 1.6 \times 10^2$ Hz |
| | $n_1 = 2.0 \times 10^2$ | FWHM = $2.7 \times 10^2$ Hz |
| Cavity | $\alpha = 1.1$ | $A_0 = 2.5$ Hz |
| | $n_1 = 1.1 \times 10^3$ | FWHM = 9.4 Hz |

terms of motional narrowing by one or a few dominant RTS fluctuators. We now show how the resonator field can "sympathetically" drive two-level defects in the surrounding dielectric in a regime that results in RTS noise with the required power dependence to explain the observations. This effect of sympathetic driving of the bath of defects and the resulting motional narrowing likely influences the power dependence in many superconducting devices.

**Motional narrowing**
Together, the plots in Fig. 1 highlight the power-dependent transition from multipeaked behavior at low circulating power in the resonator to single-peaked behavior at high power. In addition, as the power increases, the widths of the histograms narrow. Such behavior is indicative of motional narrowing (motional averaging) (27), where a multilevel system transitions into a single-level system that also exhibits increased spectral stability. Motional narrowing is a common phenomenon that has been found in a wide variety of systems: nuclear magnetic resonance spectra (27, 34), electron spin resonance spectra (28), gamma emissions (29), and two-level NV center defects (35, 36). Li *et al.* (37) experimentally simulated motional narrowing of the spectroscopic transition in superconducting qubits and suggested that driving the TLS would reduce qubit dephasing; otherwise, despite the similarity between an NV center and a parasitic TLS, motional narrowing has not been considered in the

framework of dielectric loss, charge noise, or other TLS phenomena affecting superconducting circuits.

The observation of quasi-stable resonant frequencies is consistent with the model of a bath of spectrally unstable, charged TLS that are dispersively coupled to the resonator (7, 12, 38, 39). In previous studies of resonators, the coupling to many TLS manifested as a $1/f$ noise spectrum (38, 40, 41). Within studies on superconducting qubits, the coupling to TLS has been strong enough to result in an RTS noise spectrum (9, 13). The RTS noise behavior found here demonstrates a similar coupling to single or few individual TLS.

Typically, in such a model of dispersively coupled (near-resonant) TLS, their dynamics are dominated by incoherent, low-frequency two-state fluctuators whose fluctuations dephase the TLS (widen its spectrum) or shift the TLS energy (11, 38, 39, 42). This results in a $1/f$ noise spectrum that scales as approximately $1/\sqrt{\langle n \rangle}$. Here, we see single or few RTS dynamics rather than $1/f$ noise, where the RTS amplitude scales as $1/\sqrt{\langle n \rangle}$ (Fig. 3A) up until some critical power, beyond which it becomes power independent. However, a very clear nearly $1/\langle n \rangle$ dependence of $\tau_0$ (Fig. 3B) over all powers suggests that the switching rate requires a different interpretation.

To understand the ramifications of the observed power dependence, we consider an RTS system with only two states, at frequencies $\pm A$, with a characteristic switching rate between these states of $W$ per unit time. For slow switching, $W \ll |A|$, the spectral response of the RTS signal consists of two peaks at frequencies $\pm A$ with a width (FWHM) given by $W$. In the opposite limit of strong driving, $W \gg |A|$, the resonance is a single peak centered at zero frequency with FWHM width $A^2/W$, which is narrower. Motional narrowing can extend beyond the simple two-state to one-state example that we have described (27); in multiple-state examples (28, 29), multiple $W$ and $\pm A$ exist, although the convergence toward a single narrow state still occurs in the strong driving limit (30, 31), which is the regime we focus on. The observation that $\tau_0 \propto 1/\langle n \rangle^{1.1}$ in the fast fluctuation limit therefore suggests that $W \propto \langle n \rangle^{1.1}$, and this observation is common across all three devices.

**Landau-Zener transitions in the bath of TLS defects**
To investigate the mechanism for modulation of the TLS defect by the resonator and to explain the results presented above, we start from the assumption that the bath of fluctuators driving the RTS

behavior is described by the standard tunneling model (7, 43), where each defect can be described by the TLS Hamiltonian

$$\hat{\mathcal{H}}_0 = (-h/2)(\varepsilon\hat{\sigma}_z + \Delta_0\hat{\sigma}_x) \qquad (2)$$

as illustrated in Fig. 4. The tunnel coupling $\Delta_0$ and bias $\varepsilon$ vary from defect to defect and are a function of the local atomic environment. We assume that the electric field of the resonator couples to the defects via their charge dipole, i.e., longitudinally (along $\hat{\sigma}_z$) in the basis of uncoupled double wells. The bias is therefore composed of a constant offset and a time-dependent term

$$\varepsilon(t) = \varepsilon_0 + \varepsilon_{rf}\cos(2\pi f_r t) \qquad (3)$$

where $\varepsilon_{rf}$ has units of frequency but is proportional to the amplitude of the resonator electric field, $\propto \sqrt{\langle n \rangle}$, and hence to the radio frequency (rf) voltage at the source.

For low-loss devices, there are relatively few defects with values of $\Delta_0$ close to the resonator frequency (12, 44, 45); however, that is not the parameter regime we are considering. There are also TLS whose $\Delta_0$ is relatively small but whose equilibrium position (given by $\varepsilon_0$) is such that their eigenstates are nearly resonant with the resonator (see Fig. 4). For large resonator fields, the drive can sweep the fluctuator through the TLS anticrossing ($\varepsilon_{rf} \approx \varepsilon_0$) or at least near it. We therefore need to consider the role of Landau-Zener tunneling, which can result in transitions between the ground and excited states of the TLS (46, 47).

We can rewrite the Hamiltonian (Eq. 2) above in a time-dependent rotating frame to obtain

$$\hat{\mathcal{H}}_{RF} = (-h/2)(\delta\hat{\sigma}_{\tilde{z}} + \Delta_0 J_1(\lambda)\hat{\sigma}_{\tilde{x}}) \qquad (4)$$

where $\delta = \varepsilon_0 - f_r$ is the detuning between drive and frequency splitting at the bias point $\varepsilon = \varepsilon_0$, $J_1(\lambda)$ is the first-order (one photon) Bessel function of the first kind, representing a dressed gap, and $\lambda = \varepsilon_{rf}/f_r$ is the ratio of driving amplitude to driving frequency (46).

The relevant regime of Landau-Zener driving of TLS in the dielectric of the resonators is that the effective transition rate $W$ between states is less than the dephasing rate ($\Gamma_2$) but greater than the relaxation rate ($\Gamma_1$), i.e., $\Gamma_1 < W < \Gamma_2$. The second inequality is justified since we expect little coherence between the two eigenstates away from degeneracy, due to the dephasing that increases linearly with bias $\varepsilon$ and can amount to several megahertz (48). While this may be slower than the drive frequency, the more important comparison is to the effective Rabi frequency, which is slower, and markedly reduced away from the degeneracy point. In this regime, at resonance ($\delta = 0$) in the small-amplitude drive limit ($\varepsilon_{rf} \ll f_r$), the one-photon transition rate between the eigenstates is (49)

$$W(\lambda) = \frac{\pi^2}{2}\frac{\Delta_0^2\lambda^2}{\Gamma_2} \qquad (5)$$

Therefore, we can consider $W(\lambda)$ as the RTS switching rate, i.e., $\tau_0 = 1/W(\lambda)$, which means that $\tau_0 \propto 1/\varepsilon_{rf}^2 \propto 1/\langle n \rangle$, where the proportionality constant ($n_1$ in Eq. 1) is a product of three unknowns: the decoherence rate, the energy splitting, and the electric field amplitude at the site of the TLS. As a caveat, if there were some partial coherence in the Landau-Zener transitions, then any resulting oscillatory response in the TLS population would be averaged out with our measurement method, as we cannot control the drive phase affecting the TLS. Irrespective of the exact regime, $W \propto \Delta_0^2\lambda^2$.

We note that our observed transition rate has a small additional contribution as the amplitude is increased (cf. the exponent $\alpha = 1.1$ in Eq. 1 found empirically for all three resonators). We may attribute this to the TLS having a sufficiently large response to the resonator field that higher photon number transitions are non-negligible.

The role of Landau-Zener driving of TLS in the dielectric of qubits and resonators has been previously studied (50–52); however, in such experiments, the mechanism is modulating the frequency splitting of near-resonant TLS as they traverse the resonator frequency, thereby driving nonadiabatic Landau-Zener transitions.
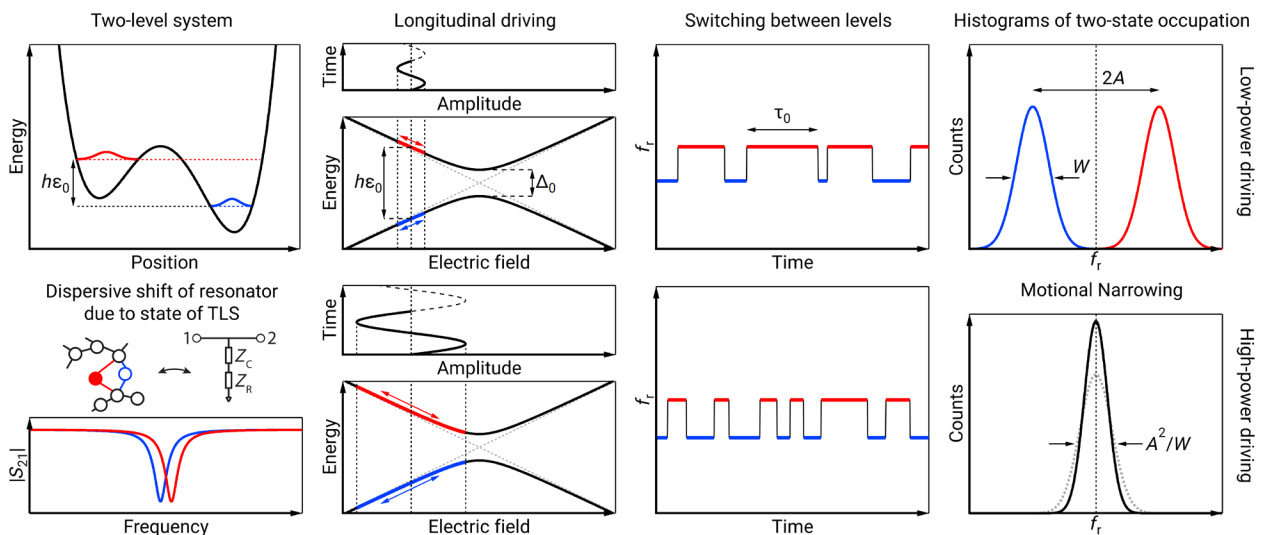
**Fig. 4. Physical model of a driven TLS leading to motional narrowing.** An illustration of the relevant RTS switching regimes (high- and low-power driving) resulting from small- and large-amplitude driving of a TLS about a bias point $\varepsilon_0$ near (but not at) its degeneracy point $\varepsilon = 0$. The resulting transitions between the two eigenstates of the TLS result in different dispersive shifts of the resonator, resulting in RTS fluctuations of the resonant frequency.

The transitions we consider (away from the degeneracy point) influence the dephasing noise (i.e., the low-frequency, real part of the spectral function), similarly to Bluvstein *et al.* (*36*), whereas Matityahu *et al.* (*50*) deals with the loss (i.e., the near-resonant, imaginary part leading to energy relaxation).

### The role of the ensemble

While this picture explains the common response between devices and the power dependence of $\tau_0$, it does not explain the low-power response of $A$ nor the "more conventional" (but less universal) response of the FWHM. However, both can be explained in terms of the ensemble of RTS fluctuations stemming from multiple TLS. As the power is reduced, below the point of coalescence in the motional narrowing picture, the fit to a single RTS fluctuator no longer captures the key characteristics of the response. The contributions from both additional RTS sources and other noise processes start to dominate, and this results in an additional power dependence to the noise amplitude. The diagonal lines in Fig. 3A represent a $1/\sqrt{\langle n \rangle}$ scaling, which one would typically expect for $1/f$ noise, indicating that, at lower powers, the ensemble response is more dominant. Similarly, the extracted FWHM in Fig. 1 (E to G) is a function of the entire spectrum, which includes both additional (non-TLS) processes and contributions due to the TLS-TLS interactions in the bath (*39*, *53–55*). As these contributions depend on the density and interaction strength between the TLS, they vary more between devices, resulting in the differing power response, cf. table S1.

In conclusion, we have studied the frequency noise of three commonly used superconducting resonators within the same measurement and analysis infrastructure. We find that, in all devices, the noise is described by an RTS process, which we attribute to spectrally unstable TLS. When studying the RTS behavior with microwave drive power, we find that the switching times follow a common scaling across all types of resonators. We interpret the power dependence of the RTS switching times in terms of sympathetic driving of TLS defects by the resonator field. This driving induces Landau-Zener–type resonant transitions, even for TLS whose equilibrium configuration is relatively detuned from the degeneracy point between the two states.

Fundamentally, this highlights the power of standardized testing with common methods. Here, the ability to directly compare different types of superconducting resonator has revealed a commonality of the dominant noise process. These findings expand the toolkit and material parameter range for examining parameter fluctuations, which has become the leading problem in superconducting quantum computing efforts. Furthermore, the studies of the nanowire superinductor are particularly relevant to the rapidly growing area of high-impedance qubits (*19*, *56–58*).

## MATERIALS AND METHODS
### Experimental design
#### Device characteristics

The examined resonators have similar resonant frequencies, but otherwise have very different superconducting properties and microwave electric field distributions. The superinductor consists of a disordered NbN nanowire with high kinetic inductance, and consequently high characteristic impedance $Z_c$, on a Si substrate. The coplanar waveguide resonator was made of Al on Si. The stub-geometry 3D cavity was machined out of 4N-grade Al. The device characteristics of the three resonators are summarized in Table 1, and their designs and fabrication techniques are thoroughly described in the given references.

The internal quality factors, $Q_i$, of the nanowire and the coplanar waveguide were determined at an average photon occupation number of $\langle n \rangle = 1$, whereas that of the cavity was determined at $\langle n \rangle = 132$ (the lowest measured); in all cases, this photon occupation corresponds to when $Q_i$ has saturated to a low level, consistent with the depolarization of two-level defects (see fig. S2). We determine $\langle n \rangle$, knowing the applied drive power $P$ and the $Q_i$ at that power, $Q_i(P)$, using the relation

$$h f_r \langle n \rangle = Z_0 Q_l^2 P / \pi^2 Z_c Q_c f_r \quad (6)$$

Here, $h$ is Planck's constant, $f_r$ is the resonant frequency, $Z_0 = 50$ ohm is the impedance of the feedline, and $Q_c$ and $Q_l$ are the coupling and loaded quality factors, respectively, with $Q_l^{-1} = Q_c^{-1} + Q_i^{-1}(P)$.

### Measurement techniques

The nanowire and coplanar resonators each exhibit a resonance dip due to coupling to a microwave transmission line. The use of a circulator at the cavity input leads to the cavity also exhibiting a resonance dip. The Pound frequency–locked loop is locked to this resonance dip. We measure the resonant frequency fluctuations by sampling the frequency of the Pound frequency–locked loop voltage-controlled oscillator using a frequency counter (Keysight 53230A) at a sampling rate of either 100 Hz or 4 kHz. Each noise trace consists of $1 \times 10^6$ samples. In addition, once per noise trace, the absolute frequency, and microwave power of the signal going into the cryostat are measured with a spectrum analyzer (Agilent E4440A). During a measurement, the cryostat temperature is held constant, and noise traces are recorded at various inbound microwave powers. A detailed description of these measurement techniques is found in (*19*, *59*).

### Statistical analysis
#### Spectral and Allan analysis of fluctuations

The same raw frequency fluctuations data are used to produce the spectrum of frequency fluctuations $S_y(f)$, using the Welch PSD estimate with 50% overlap and a Hamming window, and the overlapping Allan deviation $\sigma_y(\tau)$. A detailed description of this data analysis technique is given in (*9*, *60*).

The spectral response of a single RTS fluctuator is given by

$$S_y(f) = \frac{4 A^2 \tau_0}{1 + (2\pi f \tau_0)^2} \quad (7)$$

where $A$ and $\tau_0$ denote the RTS amplitude and characteristic time, respectively. The corresponding Allan deviation is given in (*32*)

$$\sigma_y(\tau) = \frac{A \tau_0}{\tau} \left( 4 e^{-\tau/\tau_0} - e^{-2\tau/\tau_0} + 2\frac{\tau}{\tau_0} - 3 \right)^{1/2} \quad (8)$$

A key strength of the Allan analysis is that it often allows the identification of $\tau_0$ against the noise background, although we use the same parameters when fitting $S_y(f)$ and $\sigma_y(\tau)$.

#### Estimate of errors

In the determination of $\tau_0$ and $A$ (circles in Fig. 3), we estimate the two SD errors to be about 4% (10%) for $\tau_0$ (for $A$) for the coplanar and cavity resonators and for the nanowire resonator at high powers.

For the low-power data of the nanowire resonator, we estimate about a factor of two errors in both $\tau_0$ and $A$. The collection of longer sets of data would reduce the error.

## SUPPLEMENTARY MATERIALS

Supplementary material for this article is available at https://science.org/doi/10.1126/sciadv.abh0462

## REFERENCES AND NOTES

1. J. Zmuidzinas, Superconducting microresonators: Physics and applications. *Annu. Rev. Condens. Matter Phys.* **3**, 169–214 (2012).
2. C. R. H. McRae, H. Wang, J. Gao, M. R. Vissers, T. Brecht, A. Dunsworth, D. P. Pappas, J. Mutus, Materials loss measurements using superconducting microwave resonators. *Rev. Sci. Instrum.* **91**, 091101 (2020).
3. X. Gu, A. F. Kockum, A. Miranowicz, Y.-x. Liu, F. Nori, Microwave photonics with superconducting quantum circuits. *Phys. Rep.* **718-719**, 1–102 (2017).
4. J. Aumentado, Superconducting parametric amplifiers: The state of the art in Josephson parametric amplifiers. *IEEE Microw. Mag.* **21**, 45–59 (2020).
5. A. Romanenko, D. I. Schuster, Understanding quality factor degradation in superconducting niobium cavities at low microwave field amplitudes. *Phys. Rev. Lett.* **119**, 264801 (2017).
6. A. Romanenko, R. Pilipenko, S. Zorzetti, D. Frolov, M. Awida, S. Belomestnykh, S. Posen, A. Grassellino, Three-dimensional superconducting resonators at $T < 20$ mK with photon lifetimes up to $\tau = 2$ s. *Phys. Rev. Appl.* **13**, 034032 (2020).
7. C. Müller, J. H. Cole, J. Lisenfeld, Towards understanding two-level-systems in amorphous solids: Insights from quantum circuits. *Rep. Prog. Phys.* **82**, 124501 (2019).
8. F. Yan, S. Gustavsson, A. Kamal, J. Birenbaum, A. P. Sears, D. Hover, T. J. Gudmundsen, D. Rosenberg, G. Samach, S. Weber, J. L. Yoder, T. P. Orlando, J. Clarke, A. J. Kerman, W. D. Oliver, The flux qubit revisited to enhance coherence and reproducibility. *Nat. Commun.* **7**, 12964 (2016).
9. J. J. Burnett, A. Bengtsson, M. Scigliuzzo, D. Niepce, M. Kudra, P. Delsing, J. Bylander, Decoherence benchmarking of superconducting qubits. *npj Quantum Inf.* **5**, 54 (2019).
10. A. Bruno, G. de Lange, S. Asaad, K. L. van der Enden, N. K. Langford, L. DiCarlo, Reducing intrinsic loss in superconducting resonators by surface treatment and deep etching of silicon substrates. *Appl. Phys. Lett.* **106**, 182601 (2015).
11. C. Müller, J. Lisenfeld, A. Shnirman, S. Poletto, Interacting two-level defects as sources of fluctuating high-frequency noise in superconducting circuits. *Phys. Rev. B* **92**, 035442 (2015).
12. P. V. Klimov, J. Kelly, Z. Chen, M. Neeley, A. Megrant, B. Burkett, R. Barends, K. Arya, B. Chiaro, Y. Chen, A. Dunsworth, A. Fowler, B. Foxen, C. Gidney, M. Giustina, R. Graff, T. Huang, E. Jeffrey, E. Lucero, J. Y. Mutus, O. Naaman, C. Neill, C. Quintana, P. Roushan, D. Sank, A. Vainsencher, J. Wenner, T. C. White, S. Boixo, R. Babbush, V. N. Smelyanskiy, H. Neven, J. M. Martinis, Fluctuations of energy-relaxation times in superconducting qubits. *Phys. Rev. Lett.* **121**, 090502 (2018).
13. S. Schlör, J. Lisenfeld, C. Müller, A. Bilmes, A. Schneider, D. P. Pappas, A. V. Ustinov, M. Weides, Correlating decoherence in transmon qubits: Low frequency noise by single fluctuators. *Phys. Rev. Lett.* **123**, 190502 (2019).
14. P. V. Klimov, J. Kelly, J. M. Martinis, H. Neven, The snake optimizer for learning quantum processor control parameters. arXiv:2006.04594 (2020).
15. R. Barends, J. Wenner, M. Lenander, Y. Chen, R. C. Bialczak, J. Kelly, E. Lucero, P. O'Malley, M. Mariantoni, D. Sank, H. Wang, T. C. White, Y. Yin, J. Zhao, A. N. Cleland, J. M. Martinis, J. J. A. Baselmans, Minimizing quasiparticle generation from stray infrared light in superconducting quantum circuits. *Appl. Phys. Lett.* **99**, 113507 (2011).
16. C. M. Quintana, A. Megrant, Z. Chen, A. Dunsworth, B. Chiaro, R. Barends, B. Campbell, Y. Chen, I.-C. Hoi, E. Jeffrey, J. Kelly, J. Y. Mutus, P. J. J. O'Malley, C. Neill, P. Roushan, D. Sank, A. Vainsencher, J. Wenner, T. C. White, A. N. Cleland, J. M. Martinis, Characterization and reduction of microfabrication-induced decoherence in superconducting quantum circuits. *Appl. Phys. Lett.* **105**, 062601 (2014).
17. L. Grünhaupt, N. Maleeva, S. T. Skacel, M. Calvo, F. Levy-Bertrand, A. V. Ustinov, H. Rotzinger, A. Monfardini, G. Catelani, I. M. Pop, Loss mechanisms and quasiparticle dynamics in superconducting microwave resonators made of thin-film granular aluminum. *Phys. Rev. Lett.* **121**, 117001 (2018).
18. W. Zhang, K. Kalashnikov, W.-S. Lu, P. Kamenov, T. DiNapoli, M. E. Gershenson, Microresonators fabricated from high-kinetic-inductance aluminum films. *Phys. Rev. Appl.* **11**, 011003 (2019).
19. D. Niepce, J. Burnett, J. Bylander, High kinetic inductance Nb N nanowire superinductors. *Phys. Rev. Appl.* **11**, 044014 (2019).
20. M. Kudra, J. Biznárová, A. Fadavi Roudsari, J. J. Burnett, D. Niepce, S. Gasparinetti, B. Wickman, P. Delsing, High quality three-dimensional aluminum microwave cavities. *Appl. Phys. Lett.* **117**, 070601 (2020).
21. L. Faoro, L. B. Ioffe, Quantum two level systems and kondo-like traps as possible sources of decoherence in superconducting qubits. *Phys. Rev. Lett.* **96**, 047001 (2006).
22. L. Faoro, L. B. Ioffe, Microscopic origin of low-frequency flux noise in Josephson circuits. *Phys. Rev. Lett.* **100**, 227005 (2008).
23. H. le Sueur, A. Svilans, N. Bourlet, A. Murani, L. Bergé, L. Dumoulin, P. Joyez, Microscopic charged fluctuators as a limit to the coherence of disordered superconductor devices. arXiv:1810.12801 (2018).
24. S. E. de Graaf, L. Faoro, L. B. Ioffe, S. Mahashabde, J. J. Burnett, T. Lindström, S. E. Kubatkin, A. V. Danilov, A. Y. Tzalenchuk, Two-level systems in superconducting quantum devices due to trapped quasiparticles. *Sci. Adv.* **6**, eabc5055 (2020).
25. D. Niepce, J. J. Burnett, M. G. Latorre, J. Bylander, Geometric scaling of two-level-system loss in superconducting resonators. *Supercond. Sci. Technol.* **33**, 025013 (2020).
26. M. Reagor, H. Paik, G. Catelani, L. Sun, C. Axline, E. Holland, I. M. Pop, N. A. Masluk, T. Brecht, L. Frunzio, M. H. Devoret, L. Glazman, R. J. Schoelkopf, Reaching 10ms single photon lifetimes for superconducting aluminum cavities. *Appl. Phys. Lett.* **102**, 192604 (2013).
27. A. Abragam, *Principles of Nuclear Magnetism* (Oxford Univ. Press, 1961).
28. P. P. Borbat, A. J. Costa-Filho, K. A. Earle, J. K. Moscicki, J. H. Freed, Electron spin resonance in studies of membranes and proteins. *Science* **291**, 266–269 (2001).
29. G. J. Perlow, Influence of radio-frequency magnetic fields on the mössbauer effect in magnetic $Co^{57}$ sources. *Phys. Rev.* **172**, 319–324 (1968).
30. A. Berthelot, I. Favero, G. Cassabois, C. Voisin, C. Delalande, P. Roussignol, R. Ferreira, J. M. Gérard, Unconventional motional narrowing in the optical spectrum of a semiconductor quantum dot. *Nat. Phys.* **2**, 759–764 (2006).
31. G. Cassabois, in *Spectral diffusion, dephasing and motional narrowing in single semiconductor quantum dots, NanoScience and Technology* (Springer, Berlin, 2010), pp. 25–35.
32. C. M. Van Vliet, P. H. Handel, A new transform theorem for stochastic processes with special application to counting statistics. *Physica A* **113**, 261–276 (1982).
33. C. D. Nugroho, V. Orlyanchik, D. J. Van Harlingen, Low frequency resistance and critical current fluctuations in Al-based Josephson junctions. *Appl. Phys. Lett.* **102**, 142602 (2013).
34. T. Kohmoto, Y. Fukuda, M. Kunitomo, K. Ishikawa, M. Tanigawa, K. Ebina, M. Kaburagi, Hole burning in well-defined noise fields: Motional narrowing. *Phys. Rev. B* **49**, 15352–15355 (1994).
35. L. Jiang, M. V. G. Dutt, E. Togan, L. Childress, P. Cappellaro, J. M. Taylor, M. D. Lukin, Coherence of an optically illuminated single nuclear spin qubit. *Phys. Rev. Lett.* **100**, 073001 (2008).
36. D. Bluvstein, Z. Zhang, C. A. McLellan, N. R. Williams, A. C. B. Jayich, Extending the quantum coherence of a near-surface qubit by coherently driving the paramagnetic surface environment. *Phys. Rev. Lett.* **123**, 146804 (2019).
37. J. Li, M. P. Silveri, K. S. Kumar, J.-M. Pirkkalainen, A. Vepsäläinen, W. C. Chien, J. Tuorila, M. A. Sillanpää, P. J. Hakonen, E. V. Thuneberg, G. S. Paraoanu, Motional averaging in a superconducting qubit. *Nat. Commun.* **4**, 1420 (2013).
38. J. Burnett, L. Faoro, I. Wisby, V. L. Gurtovoi, A. V. Chernykh, G. M. Mikhailov, V. A. Tulin, R. Shaikhaidarov, V. Antonov, P. J. Meeson, A. Ya. Tzalenchuk, T. Lindström, Evidence for interacting two-level systems from the 1/f noise of a superconducting resonator. *Nat. Commun.* **5**, 4119 (2014).
39. L. Faoro, L. B. Ioffe, Interacting tunneling model for two-level systems in amorphous materials and its predictions for their dephasing and noise in superconducting microresonators. *Phys. Rev. B* **91**, 014201 (2015).
40. C. Neill, A. Megrant, R. Barends, Y. Chen, B. Chiaro, J. Kelly, J. Y. Mutus, P. J. J. O'Malley, D. Sank, J. Wenner, T. C. White, Y. Yin, A. N. Cleland, J. M. Martinis, Fluctuations from edge defects in superconducting resonators. *Appl. Phys. Lett.* **103**, 072601 (2013).
41. S. E. de Graaf, L. Faoro, J. Burnett, A. A. Adamyan, A. Ya. Tzalenchuk, S. E. Kubatkin, T. Lindström, A. V. Danilov, Suppression of low-frequency charge noise in superconducting resonators by surface spin desorption. *Nat. Commun.* **9**, 1143 (2018).
42. C. Müller, A. Shnirman, Y. Makhlin, Relaxation of Josephson qubits due to strong coupling to two-level systems. *Phys. Rev. B* **80**, 134517 (2009).
43. W. A. Phillips, Two-level states in glasses. *Rep. Prog. Phys.* **50**, 1657–1708 (1987).
44. J. Lisenfeld, G. J. Grabovskij, C. Müller, J. H. Cole, G. Weiss, A. V. Ustinov, Observation of directly interacting coherent two-level systems in an amorphous material. *Nat. Commun.* **6**, 6182 (2015).
45. J. Lisenfeld, A. Bilmes, A. Megrant, R. Barends, J. Kelly, P. Klimov, G. Weiss, J. M. Martinis, A. V. Ustinov, Electric field spectroscopy of material defects in transmon qubits. *npj Quantum Inf.* **5**, 105 (2019).
46. W. D. Oliver, S. O. Valenzuela, Large-amplitude driving of a superconducting artificial atom. *Quantum Inf. Process.* **8**, 261–281 (2009).
47. W. D. Oliver, Y. Yu, J. C. Lee, K. K. Berggren, L. S. Levitov, T. P. Orlando, Mach-zehnder interferometry in a strongly driven superconducting qubit. *Science* **310**, 1653–1657 (2005).
48. J. Lisenfeld, A. Bilmes, S. Matityahu, S. Zanker, M. Marthaler, M. Schechter, G. Schön, A. Shnirman, G. Weiss, A. V. Ustinov, Decoherence spectroscopy with individual two-level tunneling defects. *Sci. Rep.* **6**, 23786 (2016).

49. D. M. Berns, W. D. Oliver, S. O. Valenzuela, A. V. Shytov, K. K. Berggren, L. S. Levitov, T. P. Orlando, Coherent quasiclassical dynamics of a persistent current qubit. *Phys. Rev. Lett.* **97**, 150502 (2006).

50. S. Matityahu, H. Schmidt, A. Bilmes, A. Shnirman, G. Weiss, A. V. Ustinov, M. Schechter, J. Lisenfeld, Dynamical decoupling of quantum two-level systems by coherent multiple Landau-Zener transitions. *npj Quantum Inf.* **5**, 114 (2019).

51. A. L. Burin, M. S. Khalil, K. D. Osborn, Universal dielectric loss in glass from simultaneous bias and microwave fields. *Phys. Rev. Lett.* **110**, 157002 (2013).

52. M. S. Khalil, S. Gladchenko, M. J. A. Stoutimore, F. C. Wellstood, A. L. Burin, K. D. Osborn, Landau-Zener population control and dipole measurement of a two-level-system bath. *Phys. Rev. B* **90**, 100201 (2014).

53. L. Faoro, L. B. Ioffe, Internal loss of superconducting resonators induced by interacting two-level systems. *Phys. Rev. Lett.* **109**, 157005 (2012).

54. N. Kirsh, E. Svetitsky, A. L. Burin, M. Schechter, N. Katz, Revealing the nonlinear response of a tunneling two-level system ensemble using coupled modes. *Phys. Rev. Materials* **1**, 012601 (2017).

55. A. L. Burin, A. O. Maksymov, Theory of nonlinear microwave absorption by interacting two-level systems. *Phys. Rev. B* **97**, 214208 (2018).

56. L. Grünhaupt, M. Spiecker, D. Gusenkova, N. Maleeva, S. T. Skacel, I. Takmakov, F. Valenti, P. Winkel, H. Rotzinger, W. Wernsdorfer, A. V. Ustinov, I. M. Pop, Granular aluminium as a superconducting material for high-impedance quantum circuits. *Nat. Mater.* **18**, 816–819 (2019).

57. L. B. Nguyen, Y.-H. Lin, A. Somoroff, R. Mencia, N. Grabon, V. E. Manucharyan, High-coherence fluxonium qubit. *Phys. Rev. X* **9**, 041041 (2019).

58. T. M. Hazard, A. Gyenis, A. Di Paolo, A. Asfaw, S. A. Lyon, A. Blais, A. A. Houck, Nanowire superinductance fluxonium qubit. *Phys. Rev. Lett.* **122**, 010504 (2019).

59. T. Lindström, J. Burnett, M. Oxborrow, A. Ya. Tzalenchuk, Pound-locking for characterization of superconducting microresonators. *Rev. Sci. Instrum.* **82**, 104706 (2011).

60. E. Rubiola, *Phase Noise and Frequency Stability in Oscillators* (Cambridge Univ. Press, 2008).

61. J. Burnett, A. Bengtsson, D. Niepce, J. Bylander, Noise and loss of superconducting aluminium resonators at single photon energies. *J. Phys. Conf. Ser.* **969**, 012131 (2018).

62. P. Macha, S. H. W. van der Ploeg, G. Oelsner, E. Il'ichev, H.-G. Meyer, S. Wünsch, M. Siegel, Losses in coplanar waveguide resonators at millikelvin temperatures. *Appl. Phys. Lett.* **96**, 062503 (2010).

63. D. S. Wisbey, J. Gao, M. R. Vissers, F. C. S. da Silva, J. S. Kline, L. Vale, D. P. Pappas, Effect of metal/substrate interfaces on radio-frequency loss in superconducting coplanar waveguides. *J. Appl. Phys.* **108**, 093918 (2010).

64. H. Paik, K. D. Osborn, Reducing quantum-regime dielectric loss of silicon nitride for superconducting quantum circuits. *Appl. Phys. Lett.* **96**, 072505 (2010).

65. J. Burnett, J. Sagar, O. W. Kennedy, P. A. Warburton, J. C. Fenton, Low-loss superconducting nanowire circuits using a neon focused ion beam. *Phys. Rev. Appl.* **8**, 014039 (2017).

66. A. Bilmes, S. Zanker, A. Heimes, M. Marthaler, G. Schön, G. Weiss, A. V. Ustinov, J. Lisenfeld, Electronic decoherence of two-level systems in a Josephson junction. *Phys. Rev. B* **96**, 064504 (2017).

**Citation:** D. Niepce, J. J. Burnett, M. Kudra, J. H. Cole, J. Bylander, Stability of superconducting resonators: Motional narrowing and the role of Landau-Zener driving of two-level defects. *Sci. Adv.* **7**, eabh0462 (2021).

**View the article online**
**Permissions**

Use of think article is subject to the Terms of service